Photochemical & Photobiological Sciences (2021) 20:715–732
https://doi.org/10.1007/s43630-021-00045-7

ORIGINAL PAPERS

Ultrafast proton release reaction and primary photochemistry of phycocyanobilin in solution observed with fs-time-resolved mid-IR and UV/Vis spectroscopy

Maximilian Theiß[1] · Merten Grupe[1] · Tilman Lamparter[2] · Maria Andrea Mroginski[3] · Rolf Diller[1]

Received: 29 January 2021 / Accepted: 16 April 2021 / Published online: 17 May 2021

Abstract
Deactivation processes of photoexcited (λ_{ex} = 580 nm) phycocyanobilin (PCB) in methanol were investigated by means of UV/Vis and mid-IR femtosecond (fs) transient absorption (TA) as well as static fluorescence spectroscopy, supported by density-functional-theory calculations of three relevant ground state conformers, PCB_A, PCB_B and PCB_C, their relative electronic state energies and normal mode vibrational analysis. UV/Vis fs-TA reveals time constants of 2.0, 18 and 67 ps, describing decay of PCB_B*, of PCB_A* and thermal re-equilibration of PCB_A, PCB_B and PCB_C, respectively, in line with the model by Dietzek et al. (Chem Phys Lett 515:163, 2011) and predecessors. Significant substantiation and extension of this model is achieved first via mid-IR fs-TA, i.e. identification of molecular structures and their dynamics, with time constants of 2.6, 21 and 40 ps, respectively. Second, transient IR continuum absorption (CA) is observed in the region above 1755 cm^{-1} (CA1) and between 1550 and 1450 cm^{-1} (CA2), indicative for the IR absorption of highly polarizable protons in hydrogen bonding networks (X–H···Y). This allows to characterize chromophore protonation/deprotonation processes, associated with the electronic and structural dynamics, on a molecular level. The PCB photocycle is suggested to be closed via a long living (> 1 ns), PCB_C-like (i.e. deprotonated), fluorescent species.

Keywords Phycocyanobilin · Bilin · Photochemistry · Ultrafast spectroscopy · Infrared continuum absorption · Proton transfer

1 Introduction

Phycocyanobilin (PCB) is an open chain tetrapyrrole and an important member of the bilin family, which is widely spread in nature [1]. When bound to proteins, bilins serve as chromophores in plant phytochromes (phytochromobilin), important bacterial and fungi sensor proteins (biliverdin), as well as in cyanobacterial phycocyanin (PCB) to trigger essential biological functions like plant growth and flower formation, or to collect solar energy via e.g. chromophore Z/E isomerization and protonation processes [2–7]. Also the use of artificial phytochromes as fluorescent biomarkers is an auspicious approach [8]. Furthermore, the application of PCB in the promising field of optogenetics [9] and as molecular switch [10] is conceivable. For all applications, a deep understanding of the properties of PCB is crucial, especially regarding conformation and protonation state, as well as the photoinduced reactions when bound to phycobiliproteins and, therefore, in particular in the free, unbound form in solution.

The basic structure of PCB is formed by four pyrrole rings that are linked via methine bridges [1]. The molecule in its unbound form is characterized by a high degree of conformational flexibility due to rotation around the single bonds of these bridges [11]. The chemical structure of PCB in the cyclic helical all-Z, all-syn (sss) conformation is

Pushing the limits of flash photolysis to unravel the secrets of biological electron and proton transfer - a topical issue in honour of Klaus Brettel.

✉ Rolf Diller
diller@physik.uni-kl.de

[1] Physics Department, TU Kaiserslautern, Erwin-Schrödinger-Straße 46, 67663 Kaiserslautern, Germany

[2] Botanical Institute, Karlsruhe Institute of Technology, Fritz Haber Weg 4, 76131 Karlsruhe, Germany

[3] Institute of Chemistry, TU Berlin, Straße des 17. Juni 135, 10623 Berlin, Germany

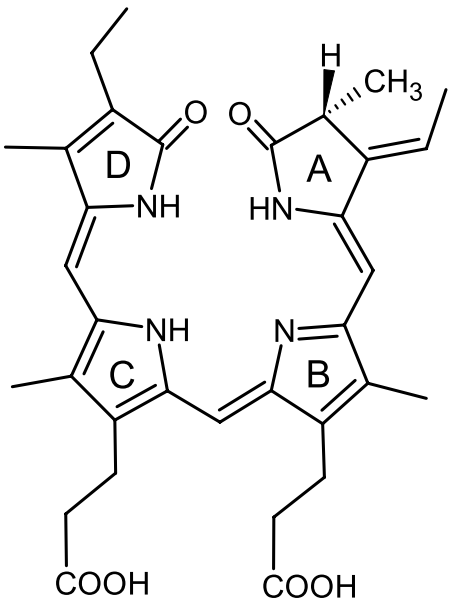

Fig. 1 Chemical structure of PCB in cyclic helical all-Z, all-syn (sss) arrangement, which is the most stable conformation in thermal equilibrium at room temperature in methanol (MeOH)

shown in Fig. 1 (Z and syn regarding double bond and single bond of the methine bridges between ring A and B, B and C, C and D, respectively).

The complex structural manifold of PCB in solution is not fully understood and has been focus of numerous theoretical and experimental studies: early mass spectrometric, static IR and NMR measurements revealed a first characterization of the molecular structure of PCB [12, 13], followed by further NMR studies that suggested a cyclic helical arrangement as the most stable structure in MeOH(-d_4) [14, 15] and a shift to more stretched geometries after protonation [15]. To further elucidate the molecular properties of PCB, theoretical studies on model bilindiones and PCB, focussing on the possible conformers by rotating around single and double bonds of the methine bridges (excluding solvent environment), support the cyclic helical all-Z, sss conformation as the most stable structure, while additionally some more stretched species yield local energy minima with sufficiently low energy barriers to possibly coexist at room temperature [16–18]. Furthermore, the solvent environment has a strong influence on the complex structural manifold of PCB [10, 19].

Considering also the protonation state and processes, which play a crucial role in the photoconversion of phytochromes [20–27] and significantly change the spectral properties of the PCB molecule, Göller and co-workers, via semiempirical AM1 calculations, found three possible all-Z ground state species (in accordance with further experimental results, see below), which are depicted in Fig. 2 [18, 28]. The cyclic helical sss conformation (PCB_A) in Fig. 2a is unprotonated with only one unprotonated pyrroleninic nitrogen atom. The more stretched ass conformation (PCB_B) in Fig. 2b is supposed to be protonated with all nitrogen atoms protonated, and the sas conformation (PCB_C) in Fig. 2c) presumably is deprotonated with two unprotonated pyrroleninic nitrogen atoms.

These results are not experimentally confirmed in detail. However, a profound knowledge of the properties of the PCB ground state species as well as its propensity for de/protonation processes after photoexcitation is crucial for a detailed understanding of the complex photoinduced molecular reactions.

Fundamental and systematic experimental studies in this direction have been undertaken using excitation wavelength dependent fs-TA spectroscopy in the visible and NIR spectral region in various solvents, as well as time resolved fluorescence measurements and transient population grating spectroscopy [29–32]. On this solid basis, a set of photoinduced reactions of the three ground state species of PCB in MeOH has been suggested as follows. PCB_B* and PCB_C* decay to their respective ground states within a few picoseconds. PCB_A* decays in parallel to PCB_A, PCB_B and PCB_C on the time scale of about 30 ps. Here, PCB_B is formed via rotation of ring A around the ring A/ring B methine bridge single bond as well as

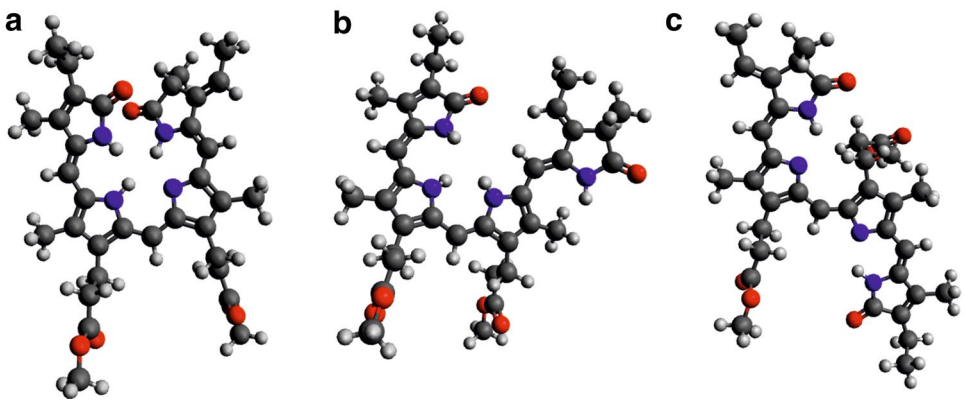

Fig. 2 Assumed conformations and protonation states of the ground state species of PCB according to Ref. [18, 28]. Grey: carbon; white: hydrogen; blue: nitrogen; red: oxygen. **a** all-Z sss conformation, unprotonated (PCB_A); **b** all-Z ass conformation, protonated (PCB_B); **c** all-Z, sas conformation, deprotonated (PCB_C)

protonation, whereas PCB_C is formed via rotation of ring A and B around the ring B/ring C methine bridge single bond as well as deprotonation of the sss chromophore PCB_A*. The proposed disproportionation reaction is also supported by quantum-chemical calculations [28]. The recovered population of the three ground state species equilibrates thermally on the timescale of 170–350 ps. Finally, via this kinetic model, the absorption spectra of the three ground state species PCB_A, PCB_B and PCB_C in thermal equilibrium at room temperature in MeOH were modelled quantitatively (cf. Figure 2).

However, the identification of the proposed processes in the visible and near-IR spectral region is difficult due to their complex influence on the TA properties and the overlapping absorption spectra of the ground state species. Thus, for a more detailed characterization of the primary photoinduced processes of PCB, in this work we performed fs-TA measurements in the mid-IR spectral region, which monitors structural changes and is sensitive to protonation processes and intermolecular interactions [33–38]. The measurements are complemented by DFT calculations for the basic ground state structures (Fig. 2) and energies, as well as for respective normal mode analysis and IR-spectra. Together with fs-TA measurements in the visible spectral region to verify and complement the existing reaction model, and with static 2D fluorescence experiments, a new detailed kinetic model of the photoreactions of PCB in MeOH solution is presented.

2 Materials and methods

2.1 Sample preparation

The extraction of PCB from *spirulina geitlerie* and purification via HPLC have been described earlier [39]. For the mid-IR measurements, the sample (PCB in MeOH, UVASOL grade, neutral pH) was additionally rebuffered to MeOH-d_4 (≥ 99.8 atom % D, purity ≥ 99%, neutral pH) using a rotary evaporator.

For UV/Vis fs-TA measurements, PCB dissolved in MeOH with OD ≈ 0.75 at the excitation wavelength of 580 nm and an optical path of 0.5 mm was used, corresponding to a concentration of ca. 0.7 mM. For all transient experiments, the solution was filled between two CaF_2-windows with an appropriate spacer.

For fs-TA mid-IR measurements, PCB dissolved in MeOH-d_4 (instead of MeOH with insufficient IR-transmission) with OD 0.75–1 at the excitation wavelength of 580 nm and an optical path of 0.25 mm (CaF_2-cuvette) was used, corresponding to concentrations of ca. 1.4–1.9 mM.

For both experiments, the samples were rotated and moved perpendicular to the laser beam to reduce and control sample integrity (cf. SI) and maintain fresh sample conditions. All measurements were performed at room temperature.

2.2 Static measurements

The static UV/Vis absorption spectra were recorded with a Jasco-V670 spectrometer, using the same cuvette and sample as for UV/Vis fs-TA measurements (cf. above).

The static 2D fluorescence measurements (excitation/emission spectra) were performed with a Perkin-Elmer LS 55 fluorescence spectrometer. Quartz glass cuvettes with a path length of 1 mm were used (PCB in MeOH-d_4 with OD ≈ 0.05 at 580 nm, corresponding to concentration 17 µmol/L). Spectrometer step-width was set to 5 nm, with excitation and emission bandwidth each set to 10 nm. For the determination of PCB concentration, an extinction coefficient of $21100 \pm 2000\ M^{-1}\ cm^{-1}$ was used (cf. Fig. S7).

The static IR measurements were carried out with a Nicolet 380 FTIR spectrometer (Thermo Electron Corporation) with an AT-IR experimental setup. For this, a droplet of PCB dissolved in MeOH-d_4 (OD 1 at 580 nm and 0.25 mm optical path, as used for the transient mid-IR measurements) was used.

2.3 Transient UV/Vis measurements

The UV/Vis fs-TA pump-probe measurements were performed based on a Ti:Sa chirped pulse regenerative amplifier system (Coherent Libra, 100 fs pulse duration (full width at half maximum (FWHM)), 4 mJ/pulse at 800 nm, 1 kHz repetition rate). The excitation pulses with 400 nJ per pulse at 580 nm were generated by a home-built two stage NOPA (non-collinear parametric amplifier). The focal width was ≈ 240 µm (FWHM) at sample position and the system response time was ≈ 100 fs.

The probe pulses (broad spectral continuum) were generated via self-phase-modulation in a moved CaF_2-window and had a focal width of ≈ 50 µm at sample position. The probe pulses were spectrally dispersed and detected with an integrated 512-pixel PDA camera device (Stresing).

For time delay (up to 500 ps) between pump and probe pulse, a delay stage (Physik Instrumente, PI) was used and each second pump pulse was blocked by a chopper to obtain pump-induced absorbance changes. Pump and probe pulse polarizations were superimposed in magic angle configuration at sample position.

2.4 Transient mid-IR measurements

The mid-IR fs-TA pump-probe measurements were performed based on a Ti:Sa chirped pulse amplifier system (Clark-MXR, CPA 2001, ≈ 150 fs pulse duration (FWHM), 0.78 mJ/pulse at 775 nm, 988 Hz repetition rate). The excitation pulses with 260–300 nJ per pulse at 580 nm were generated analogously to the transient UV/Vis measurements (cf. Section 2.3.). The focal width was ≈ 250 µm at sample position and the system response time was ≈ 385 fs.

The probe pulses (broad-band mid-IR continuum, spectral width ca. 50–60 cm^{-1} in the measured spectral region between 1810 and 1320 cm^{-1}, focal width ≈ 140 µm at sample position) were generated by a two-stage optical parametric amplifier (OPA), followed by difference frequency generation as described in detail earlier [40].

For time delay (up to 150 ps) between pump and probe pulse (superimposed in magic angle configuration at sample position), a delay stage (Physik Instrumente, PI) was used and each second pump pulse was blocked by a chopper.

The pump-induced absorption difference data ΔA(t, λ) of the transient UV/VIS and mid-IR experiments were analysed using a multiexponential global fit function.

$$\Delta A(t,\lambda) = A_0(\lambda) + \sum_{i=1}^{N} A_i(\lambda) \cdot e^{-t/\tau_i} \quad (1)$$

with the decay-associated spectra (DAS) $A_i(\lambda)$, and the corresponding time constants τ_i. The fitting routine was started at time delay ≥ 410 fs (UV/VIS) and ≥ 730 fs (mid-IR). The latter starting point was chosen due to the longer system response time in comparison to that of the UV/VIS system and due to partly strong cross-phase modulation signals in the mid-IR data.

2.5 DFT calculations

DFT calculations were carried out with the GAUSSIAN09 program package [41] using the B3LYP exchange–correlation functional [42] and the 6-31G* basis sets. A polarizable continuum model (PCM) [43] with ($\varepsilon_r = 32.6$) was used to describe the MeOH solvent. It is noted that the relative permittivity of MeOH and MeOH-d_4 (the solvent used for the mid-IR fs-TA experiments), $\varepsilon_r = 32.6$ [44] and $\varepsilon_r = 32.7$ [45], respectively, are basically the same. The helical structural model PCB_A ("unprotonated") was constructed using the crystal geometry [46] as structural template, including the propionic side chains and assuming a deprotonated pyrrole ring B (cf. Figure 1 and 2a). Models of PCB_B and PCB_C were generated by manually adjusting the dihedral angles at the methine bridges. While PCB_B ("protonated") represents a cationic state where all pyrrole rings are protonated, PCB_c ("deprotonated") is anionic with deprotonated rings B and C (cf. Figs. 2b and c, respectively). The exchangeable hydrogen atoms, bound to the pyrroleninic nitrogens, were replaced by deuterons. While energy minimization of the three models were performed using standard optimization algorithms implemented in GAUSSIAN09 package, vibrational frequencies, normal mode analysis and estimation of IR intensities were computed with home-made software [47]. The force constants were scaled according to procedure described in [48] using a set of global scaling factors which were previously determined in [47] and [49]. This approach partially compensates the errors in the calculated force fields resulting from deficiencies of the quantum mechanical method and from the harmonic approximation. Computation of potential energy distribution (PED) matrix [50] allowed for a quantitative description of the character of the normal modes of vibration. For the representation of IR spectra, Lorentzian band-shapes with 12 cm^{-1} FWHM were used.

The relative conformational energies between PCB_A, PCB_B and PCB_C were estimated as difference of the sum of electronic and zero-point energies assuming the same protonation pattern of neutrally charged molecules.

3 Results and discussion

3.1 Static UV/Vis absorption spectrum of PCB/MeOH

Figure 3 shows the static UV/Vis ground state absorption (GSA) spectrum of PCB in MeOH, characteristic for bilins in general [1]. Here, the strong Soret band maximum is

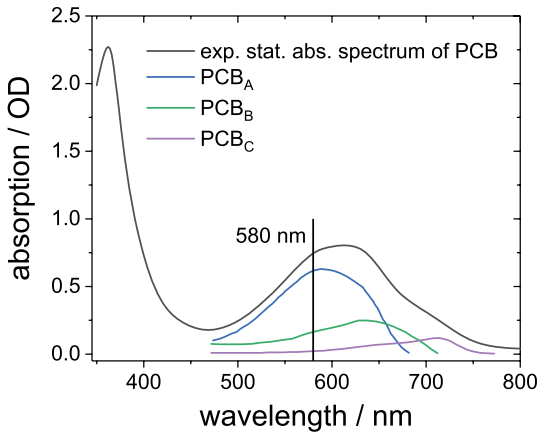

Fig. 3 Black: static UV/VIS absorption spectrum of PCB in MeOH, characterized by Soret band in the UV-, and Q-band in long-wavelength spectral region. Coloured as indicated: static Q-band absorption spectra of the ground state sub-species PCB_A, PCB_B and PCB_C, as modelled in Ref. [31]. See Fig. S1 for a comparison of the experimental static absorption spectrum and the sum of the component spectra. Excitation wavelength for UV/VIS and mid-IR fs-TA measurements at 580 nm is indicated

found at 362 nm, and the broad Q-band peaks at ca. 610 nm with a long-wavelength shoulder. In addition, the Q-band absorptions of the expected ground state sub-species of PCB, i.e. PCB_A, PCB_B and PCB_C, are given according to Ref. [31]. Pump pulse set to 580 nm for both UV/VIS- and mid-IR fs-TA measurements, leads to absorbance-weighted excitation of PCB_A, PCB_B and PCB_C, with predominant PCB_A- and negligible PCB_C-excitation.

3.2 UV/Vis fs-TA-measurements on PCB

3.2.1 Photoinduced difference spectra

Fig. 4 shows the absorption difference spectra of PCB in MeOH at selected time delays after excitation at 580 nm. Negative and positive difference signals are assigned to ground state bleaching (GSB) and excited state absorption (ESA), respectively. Here we outline the characteristic features of the transient UV/Vis data and their kinetic analysis that are the basis for and underline the already existing model, described in the introduction.

A broad GSB with a maximum at 620 nm appears immediately after photoexcitation and is accompanied by broad ESA below 550 nm and above 740 nm. GSB and ESA are assigned to superimposed respective ground and excited state absorption of PCB_A, PCB_B and PCB_C. The instantaneously rising initial difference signals decay to almost zero within ca. 200 ps over the entire spectral range, leaving a small residual difference band at long delay times, with a negative and positive peak at 585 and 685 nm, respectively. It is noted that the initial GSB fits well within the static Q-band absorption profile of PCB, albeit with smaller spectral width (due to spectral superposition with positive ESA), and shows significant variation of its spectral shape, i.e. blue-shift of the apparent minimum at 630 nm and faster decay in its red wing. This wavelength dependent recovery of the initial GSB is in line with the recovery of the spectrally distinct ground state species PCB_A, PCB_B and PCB_C after photoexcitation on different time scales as described in the following.

3.2.2 Kinetic analysis

Global analysis of the transient difference spectra is performed via Eq. (1). A triexponential fit yields time constants $\tau_1 = 2.0 \pm 0.2$ ps, $\tau_2 = 18.3 \pm 0.6$ ps and $\tau_3 = 67.0 \pm 3.0$ ps. Figure 5 shows absorbance transients at selected wavelengths and documents the high quality

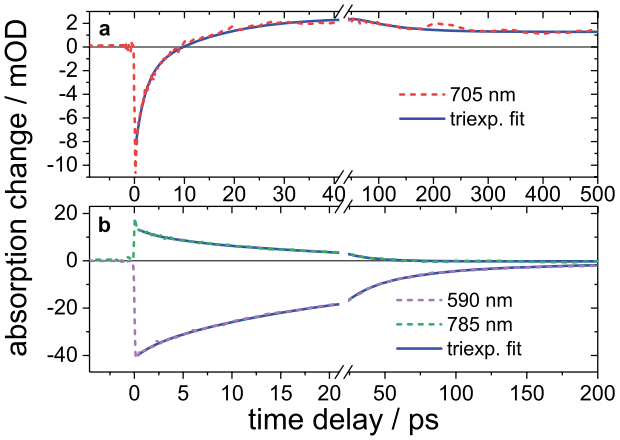

Fig. 5 Transient absorption changes (dashed lines) at selected wavelengths after excitation of PCB/MeOH at 580 nm. The blue solid lines represent the triexponential fits as described. **a** Transient absorption changes in the spectral region of the photoproduct; **b** Transient absorption changes in the spectral regions of ground state bleach and excited state absorption

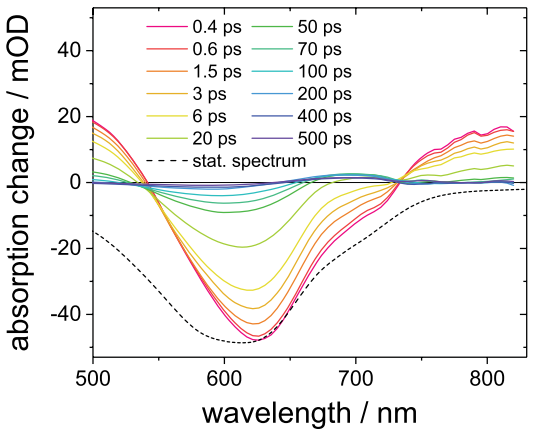

Fig. 4 Absorption difference spectra of PCB in MeOH at selected time delays after excitation at 580 nm, and the inverted static absorption spectrum (dashed)

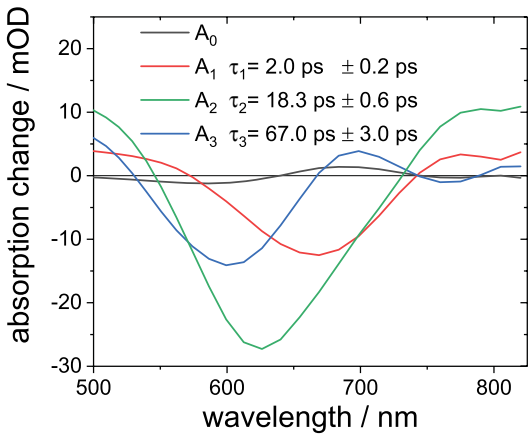

Fig. 6 Decay-associated spectra (DAS) of the kinetic components of PCB/MeOH after excitation at 580 nm as the result of global analysis. A_0 represents the residual amplitude for large delay-times and shows long-living difference signals

of the fit in the entire spectral range. For a more detailed spectro-temporal analysis of the transient difference spectra (Fig. 4) the resulting decay-associated spectra (DAS) are depicted in Fig. 6.

3.2.3 Time range of τ_1

A_1 shows positive contributions of ESA below 570 and above 744 nm. The negative band with maximum at 669 nm, i.e. in the red part of the static absorption spectrum, indicates the recovery of ground state absorption of species PCB_B (Fig. 3) with τ_1.

3.2.4 Time range of τ_2

In contrast to A_1, A_2 exhibits a broader and blue-shifted negative band, indicating contributions of more than solely one of the three ground state species (Fig. 3). This is in line with the proposed decay of PCB_A* to PCB_A, PCB_B and PCB_C on the intermediate time scale of τ_2.

3.2.5 Time range of τ_3

A_3 shows basically zero amplitude in the ESA region above 735 nm, and, below, a difference-band like pattern with peaks at 600 (neg.) and 700 nm (pos.). This correlates well with the proposed electronic ground state reaction, involving excess population of red absorbing PCB_B and PCB_C that thermally equilibrate with blue absorbing PCB_A with τ_3.

3.2.6 Long timescales

A_0 shows a small and persisting (> 0.5 ns) difference band with peaks at ca. 585 (neg.) and 685 nm (pos.). The negative band coincides well with the ground state absorption of PCB_A, indicating missing PCB_A population. The positive band we associate with a long living photoproduct, X* (justification of excited state character cf. Section 3.3), which decays finally (possibly directly) to PCB_A. It is noted that the unchanged static UV/Vis absorption spectrum of our samples after the transient measurements (cf. Fig. S6) shows the complete recovery of PCB_A and no accumulation of a new species, thereby pointing out the finite lifetime of X*.

In conclusion, the results of our UV/Vis fs-TA-measurements are comparable to those presented in Ref. [31] and [29, 32], in particular concerning transient difference spectra and their kinetic analysis. The time constant $\tau_3 = 67$ ps, revealed by our experiments, is significantly shorter than that given earlier (170–350 ps), possibly due to our explicit consideration of a long living photoproduct in comparison to Ref. [31] and [29, 32]. Our data are thus consistent with the reaction scheme proposed earlier (ibid.) and shown in Fig. 7. It additionally includes the long living photoproduct X* and serves as the working hypothesis for the following results, i.e. DFT calculations, fluorescence experiments and mid-IR fs-TA-measurements, leading to a significant development of the model.

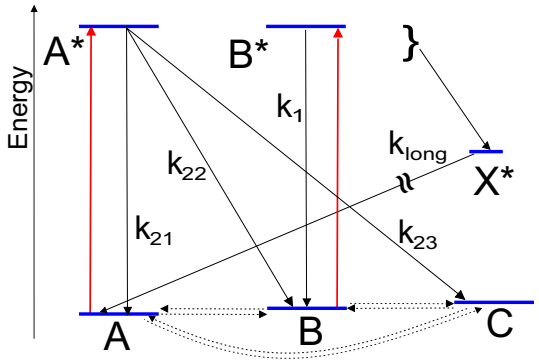

Fig. 7 Characteristic features of the kinetic scheme of the photoreaction of PCB/MeOH after excitation at $\lambda_{exc} = 580$ nm at room temperature, based on Ref. [31] and [29, 32], and consistent with our UV/VIS fs-TA-measurements. Long living photoproduct X* (justification of excited state character cf. Section 3.3) added. Red: excitation. Black: decay. Dotted: thermally driven equilibrium reactions. $(k_1)^{-1} = \tau_1$ and $(k_{21} + k_{22} + k_{23})^{-1} = \tau_2$ are the apparent time constants as revealed from the triexponential fit. τ_3 is determined by the rate constants governing the thermal equilibration between excess population of B and C with A. The long living photoproduct decays on long timescales with the rate k_{long}

3.2.7 Structural properties of DFT models and relative conformational energies

For the interpretation and analysis of experimental data, three structural models of PCB molecules with different protonation patterns were constructed: PCB_A (all-Z sss, neutrally charged and deprotonated at ring C nitrogen), PCB_B (all-Z ass, protonated all four pyrrole nitrogens) and PCB_C (all-Z sas, anionic, deprotonated at rings B and C nitrogens). DFT/PCM energy minimization of PCB_A, PCB_B and PCB_C initial structures converge to geometries characterized by the structural parameters listed in Table 1. PCB_A and PCB_B show clear helical conformations as reflected by the relatively high values of the dihedral angles (< −10°) of the methine bridges AB and CD as consequence of the steric repulsion between the protonated pyrrole ring D and the protons on rings A and C. The PCB_C structure is characterized by planar arrangements of all four rings, which results from stabilizing H-bonds between the pyrrole nitrogens of rings A and B as well as between rings C and D.

Table 1 Dihedral angles (°) and bond lengths (Å) of the methine bridges characterizing the geometry of the local energy minima of models PCB_A, PCB_B and PCB_C (cf. Fig. 16, S2 and S3 for atom numbers)

	PCB_A	PCB_B	PCB_C
Methine Bridge AB			
N38-C5-C6-C7	− 3.64	− 5.42	0.13
C4-C5-C6-C7	177.76	176.38	179.05
C5-C6-C7-N39	− 14.08	156.20	2.19
C5-C6-C7-C8	164.91	− 28.20	− 177.82
C5-C6	1.366	1.370	1.360
C6-C7	1.436	1.429	1.444
Methine Bridge BC			
N39-C10-C11-C12	− 4.90	12.64	2.91
C9-C10-C11-C12	170.83	− 163.57	− 175.56
C10-C11-C12-N40	− 4.41	12.16	175.27
C10-C11-C12-C13	176.62	− 168.96	− 2.24
C10-C11	1.380	1.390	1.397
C11-C12	1.418	1.403	1.414
Methine Bridge CD			
N40-C15-C16-C17	− 13.33	− 14.12	− 0.16
C14-C15-C16-C17	166.69	169.02	179.79
C15-C16-C17-N41	− 4.45	− 6.80	− 0.16
C15-C16-C17-C18	173.12	170.29	179.68
C15-C16	1.431	1.430	1.438
C16-C17	1.364	1.365	1.365

The relative conformational energies between the unprotonated, neutral models yielded: $E(PCB_B) - E(PCB_A) = 29$ kJ/mol and $E(PCB_C) - E(PCB_A) = 35$ kJ/mol, confirming the energetical order $E(PCB_A) < E(PCB_B) < E(PCB_C)$, found in Ref. [18] ($E(PCB_B) - E(PCB_A) = 5.5$ kJ/mol and $E(PCB_C) - E(PCB_A) = 13.0$ kJ/mol, using AM1 semiempirical approach without considering solvent effects).

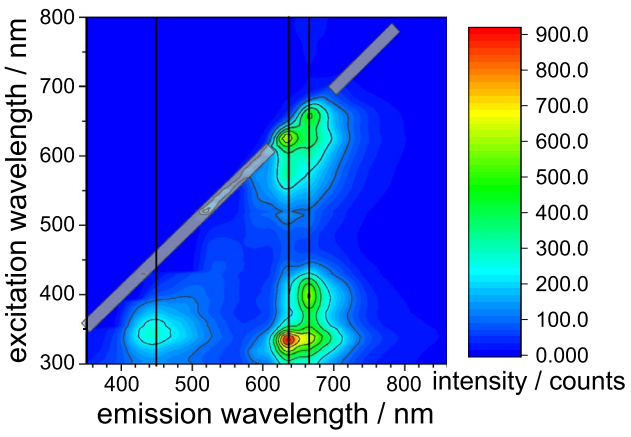

Fig. 8 Static 2D fluorescence excitation spectrum of PCB in MeOH-d_4. The vertical black lines mark the excitation spectra in Fig. 9b. Grey bar indicates scattering artefact

3.3 Static fluorescence measurements on PCB

For identification and characterization of the PCB luminescent excited states and in particular of electronic ground state heterogeneity, the results of static 2D-fluorescence excitation measurements of PCB in MeOH-d_4 are shown in Fig. 8. 1D-emission and -fluorescence excitation spectra (FES) for selected wavelengths are shown in Fig. 9a, b, respectively.

The low-energy emission around 600–700 nm, induced via excitation in the Soret- (360 nm) and Q- (600 nm) band region (Fig. 8), is assigned to PCB fluorescence. The weak, high-energy emission around 400–550 nm is assigned to a bilirubin-like chemical species, formed in MeOH(-d_4). This species exhibits shorter conjugation length owed to nucleophilic reaction at C_{10} (cf. Fig. 16 for numbering) and thus strong energetic increase of the S_0–S_1 energy gap. An analogous observation was described for biliverdin-dimethyl-ester

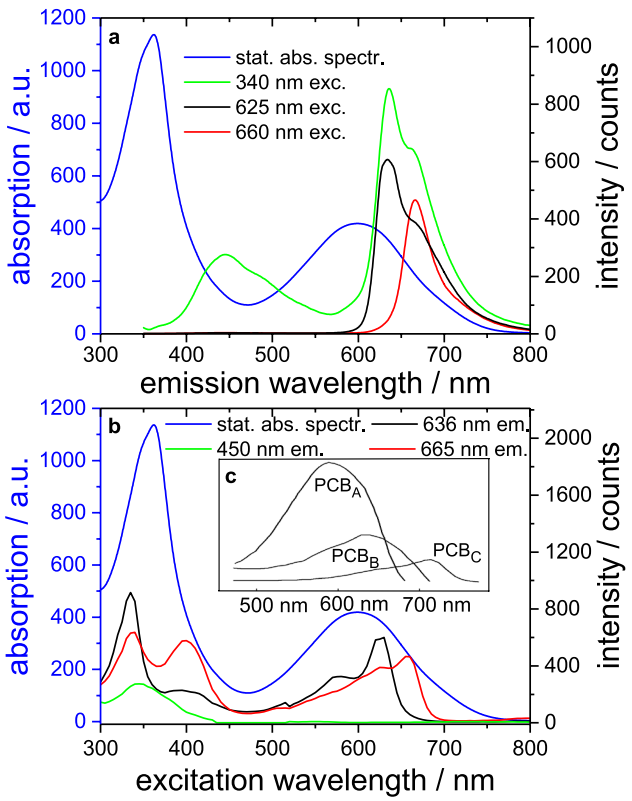

Fig. 9 **a** Static emission spectra (right black axis) for the excitation wavelengths 340 nm, 625 nm and 660 nm and the static absorption spectrum (left blue axis); **b** Static excitation spectra (right black axis) for the fluorescence emission wavelengths 450 nm, 636 nm and 665 nm and static absorption spectrum (left blue axis) for PCB in MeOH-d_4; **c** Q-band absorption spectra of PCB_A, PCB_B and PCB_C according to Ref. [31]

(BVE) in ethanol [51–54], and is expected for bilatrienes in donating solvents in general, [55] as well as via adduct formation in protein-bound forms (phytochrome [53, 56] and cyanobacteriochrome [57, 58]). It is noted that (i) in analogy to Ref. [55] this species is assumed to have a high fluorescence quantum yield, suggesting low concentration in our experiments, and (ii) that it absorbs far below our excitation wavelength of 580 nm (i.e. at 340 nm, cf. below), and thus does not contribute to the observed photoinduced fs UV/Vis and mid-IR absorbance data presented in this work.

The low-energy emission around 600–700 nm exhibits two bands with maxima at 636 and 665 nm (Figs. 8 and 9a) for both Soret- and Q-band excitation. They are assigned to excited PCB_A ($\lambda^A_{max} = 592$ nm) and PCB_B ($\lambda^A_{max} = 634$ nm) fluorescence, respectively. The corresponding Stokes shifts of 1170 cm^{-1} (44 nm, PCB_A) and 730 cm^{-1} (31 nm, PCB_B) are small and possibly affected by structure (helical vs. stretched [51]) and de-/protonation processes in PCB_A* and PCB_B* (cf. below).

In the region above 700 nm where PCB_C ($\lambda^A_{max} = 714$ nm) fluorescence could be expected, no separable emission is observed (Fig. 9a), in line with the low concentration of PCB_C and/or a low fluorescence quantum yield.

The variations of the FES (Figs. 8, and 9b) with the emission wavelength, observed in both the Soret- and the Q-band, reflect the heterogeneity of the sample. This concerns first the low-energy emission due to excited PCB_A and PCB_B with distinct absorption spectra. In particular, in the Soret region both FES shown in Fig. 9b exhibit two relatively narrow bands with maxima at the same position (340 and 400 nm), however with distinct amplitude ratios. Second, the FES of the uniform "blue" emission shows a single, similarly uniform and broader band with center of gravity around 350 nm, conform with its assignment above as a separate chemical species.

In the Q-band region of the FES (Fig. 9b) the peaks around 575 and 623 coincide quite accurately with the absorption maxima of PCB_A and PCB_B, respectively, and (the amplitudes) could possibly be related to the fluorescence quantum yield of PCB_A and PCB_B. However, this assignment is complicated by the fact that (i) the spectral widths of the corresponding emission spectra (Fig. 9a) as well as (ii) the small Stokes shifts and (iii) the difference between λ^A_{max} (PCB_A) and λ^A_{max} (PCB_B) all are of similar size (30–50 nm).

Interestingly, the FES continues to increase for wavelengths above the apparent peak of the total PCB absorption spectrum at ca. 600 nm (Fig. 9b). In particular, the FES for emission at 665 nm shows a renewed increase above λ^A_{max} (PCB_B) at 634 nm. A possible explanation for this observation could be the existence of a long-living (> 1 ns) species, generated via excitation of PCB during the fluorescence measurement. For this luminescence to become apparent, it would suffice for this species to be formed with very little quantum yield but long exited-state lifetime.

Time-resolved fluorescence measurements on PCB in MeOH with excitation at 635 nm, performed by Bischoff et al. [31], report time constants $\tau_{1,Fluo} = 2 \pm 0.8$ ps, $\tau_{2,Fluo} = 24 \pm 10$ ps and $\tau_{3,Fluo} > 1$ ns, in agreement with their transient UV/VIS measurement results, as well as with both, our fs UV/Vis time constants ($\tau_1 = 2 \pm 0.2$ ps, $\tau_2 = 18.3 \pm 0.6$ ps, $\tau_3 = 67 \pm 3$ ps and long-living photoproduct) and fs transient mid-IR measurements (cf. Section 3.5.). This is consistent with the kinetic reaction scheme in Fig. 7: The luminescent states PCB_B* and PCB_A* decay with τ_1 and τ_2. In contrast, τ_3 describes the non-radiative thermal equilibration of the electronic ground state species and is thus not found as fluorescence component. Finally, the time-constant $\tau_{3,Fluo}$ suggests the long-living species (lifetime > 500 ps, cf. above and below) found in both our fs UV/Vis is and mid-IR experiments to be an excited, fluorescent state. Although its formation quantum yield amounts to only a few percent (small amplitude around 590 nm (A_0 in Fig. 6) with respect to the initial total bleach (Fig. 4)), its long lifetime enables a high quantum yield and thus observable fluorescence intensity.

In summary, our static fluorescence and fluorescence excitation measurements clearly reveal the coexistence of differently fluorescing excited states (heterogeneity), associated with the electronic ground states PCB_A and PCB_B. Time-resolved fluorescence measurements [31] confirm PCB_A* and PCB_B* to be fluorescent states (τ_2, τ_1, resp.) and are consistent with τ_3 to describe a reaction involving non-fluorescent (electronic ground-) states. Furthermore, they suggest the long-living state (τ > 500 ps) observed and

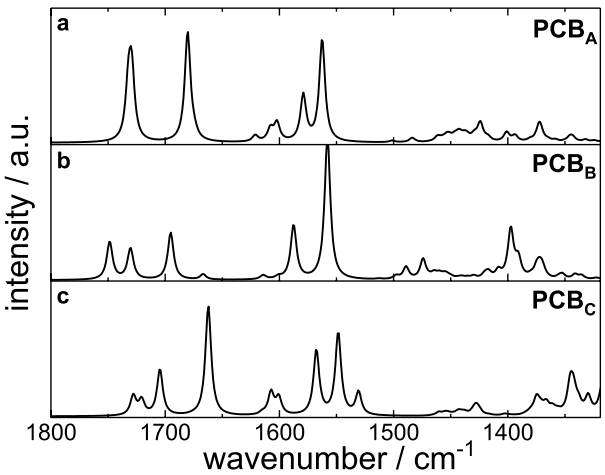

Fig. 10 Calculated static IR absorption spectra of the ground state species **a** neutral PCB_A, **b** cationic PCB_B and **c** anionic PCB_C, [28] obtained by DFT calculations with polarizable continuum model for MeOH-d_4 and deuterated pyrroleninic nitrogen atoms

characterized in our fs UV/Vis and mid-IR experiments to be a luminescent excited state.

3.4 Static IR measurements and calculated spectra

For the assignment of IR-absorption bands to molecular vibrations of specific species, the vibrational spectra of the electronic ground states PCB_A, PCB_B and PCB_C were calculated via DFT/PCM (cf. Fig. 10). Owing to their respective different structures and protonation states, the three spectra show characteristic differences throughout the complete mid-IR spectral region, covered by our fs-TA absorption measurements (ca. 1800–1320 cm^{-1}, cf. Section 3.5.). A description of significant vibrational modes is given in the main text and in Table S1.

For comparison, a weighted sum of the DFT calculated spectra (68% PCB_A, 25% PCB_B and 7% PCB_C [31]) is plotted together with the experimentally obtained, static IR absorption spectrum in MeOH-d_4 in Fig. 11. MeOH-d_4 instead of MeOH was used for the static and transient mid-IR measurements due to the insufficient IR-transmission of the latter in the investigated spectral region. However, the different solvents turn out to have no influence on the photoinduced deactivation kinetics: UV/Vis fs-TA measurements in deuterated and protonated MeOH revealed the same time constants, i.e. no influence on the photoinduced deactivation kinetics [59, 60]. Furthermore, the time constants of the fit of our transient mid-IR data in the spectral region between 1812 and 1730 cm^{-1}, measured in MeOH and in MeOH-d_4, are identical within error margins (data not shown).

The C=O str. vibrations at ring A as well as C=O str. at the propionic side chains are predicted between 1700 and 1750 cm^{-1}, while C=O str. for ring D are significantly shifted to lower wavenumbers (1670–1700 cm^{-1}, for more details cf. Table S1), in perfect agreement with the experimental static IR absorption bands at around 1709 and 1677 cm^{-1}. C=C str. modes at the methine bridges are calculated in the frequency range between ca. 1615 and 1550 cm^{-1}. Thus, they can be consequently assigned to the experimental IR absorption around 1590 cm^{-1}. Protonation of the inner-pyrrole rings, as in the case of PCB_B, induces the down shift of these modes to lower wavenumbers and a significant increase of the IR intensity. Interestingly, only for model PCB_B vibration bands with non-negligible IR intensities are predicted in the spectral window between 1430 and 1525 cm^{-1}. These vibrations are dominated by methyl HCH def. vibrations, located at ring B and C, as well as C–C and C–N str. vibrations. In models PCB_A and PCB_C, the C–N and the methyl HCH def. vibrations are significantly downshifted.

The discrepancies between the calculated and experimentally obtained spectra are most likely caused by (i) the lacking influence of intermolecular hydrogen bonds between PCB- and MeOH molecules that are not explicitly accounted for by the calculations, (ii) structural fluctuations for each of the conformers and (iii) the limitations of the harmonic approximation despite the force field scaling approach.

In conclusion, IR absorption spectra for the ground state species, obtained by DFT/PCM calculations, show characteristic differences with respect to each other and their weighted sum is in good agreement with the experimentally obtained static IR absorption spectrum. Thus, in the following, they are used to assign absorption bands in the transient mid-IR measurements to specific molecular vibrations, to distinguish between the single ground state species and, thereby, to disentangle their kinetics via vibrational fingerprints.

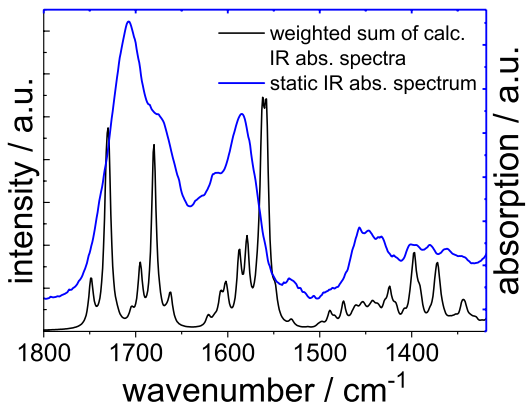

Fig. 11 Black: weighted sum of DFT/PCM calculated static IR absorption spectra (Fig. 10) of the ground state species PCB_A (68%), PCB_B (25%) and PCB_C (7%) [28]. Blue: experimentally obtained static IR absorption spectrum of PCB in MeOH-d_4

3.5 Mid-IR fs-TA-measurements on PCB

3.5.1 Photoinduced difference spectra

Mid-IR fs-TA-measurements on PCB in MeOH-d_4 were performed in the spectral region between 1810 and 1320 cm^{-1} after excitation at 580 nm, up to time delays of 200 ps. The resulting absorption difference spectra at selected time delays and, for comparison, the static IR absorption spectrum are shown in Fig. 12a and b, respectively.

The difference spectra show basically instantaneous rise of negative (GS bleach) and positive (excitation induced IR absorption) signals which decay or become stationary on the time scale of 100 ps, leaving small residual and long living (>>200 ps) difference signals. It must be noted that a satisfying match between the initial bleach spectrum (1.2 ps) and the static IR spectrum is achieved, taking into account the following aspects. First, GS vibrational modes show as

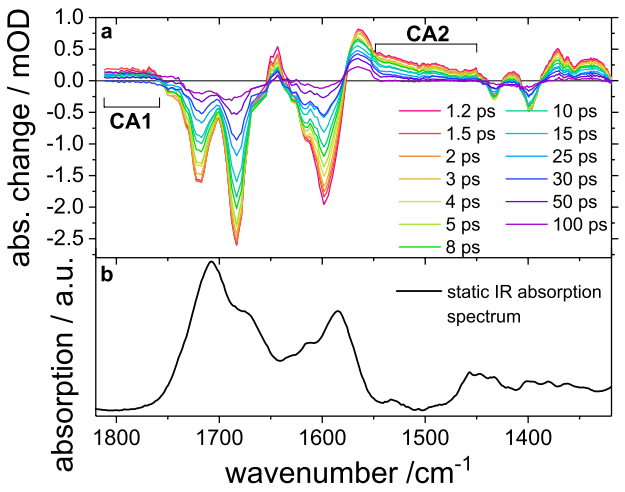

Fig. 12 **a** Absorption difference spectra of PCB in MeOH-d_4 in the spectral region between 1810 and 1320 cm^{-1} at selected time delays after excitation at 580 nm. Spectral regions of IR absorption continua CA1 and CA2 are marked (cf. text). **b** Experimental static IR absorption spectrum of PCB in MeOH-d_4 (solvent contributions subtracted)

negative signals only to the extent that they are coupled to the electronic transition and exhibit change of mode composition (frequency) or decrease of absorption cross section upon electronic excitation. Second, while the static absorption spectrum reflects the equilibrated fractions of PCB_A, PCB_B and PCB_c (cf. above), excitation at 580 nm weights (and thereby selects) the contributions of excited PCB_A, PCB_B and PCB_c according to their relative OD-value at this wavelength (Fig. 3) in the ratio of about 1.0:0.3:0.03, respectively. Third, a slight apparent spectral shift of a bleach band can be caused by its spectral overlap with a close lying positive band, and vice versa. Fourth, small bleach bands might simply be superimposed by stronger positive bands. In consequence, a match between the 1.2 ps and the static spectrum is observed as follows: the difference spectrum shows strong GS bleach bands with maxima at 1719 and 1683 cm^{-1} (C=O stretch) in the range of the broader static absorbance with peak at 1708 cm^{-1} and shoulder at 1675 cm^{-1}. The weak bleach signal at 1752 cm^{-1} is not reflected as clearly in the static spectrum. Yet, it is of unique significance as a spectrally isolated marker band (C=O stretch at ring A) for the existence of PCB_B as a protonated form (In the calculated spectra of unprotonated PCB_B, this band downshifts considerably (data not shown)). The strong bleach signal in the C=C stretch region with peak at 1600 cm^{-1} and shoulder at 1610 cm^{-1} is well matched by the static spectrum. Similarly, the weaker bleach bands at 1432 and 1398 cm^{-1} find spectral counterparts in the static spectrum. A specific band assignment of the most relevant difference signals in the context of the reaction kinetics is given below together with Fig. 14 on the basis of the DFT calculations, as well as in Table S1.

Two important observations in the difference spectra concern first the remaining bleach signals around 1719, 1683 and 1600 cm^{-1} and (positive) long-lasting product signal around 1565 cm^{-1} at 100 ps time delay, indicating the existence of a long-living photoproduct, in accordance with the corresponding observation in our UV/Vis fs-TA-measurements (cf. above). Second, two absorption continua in the spectral range above 1755 cm^{-1} (continuum absorption 1 (CA1)) and between ca. 1450 and 1550 cm^{-1} (CA2) are observed instantaneously after photoexcitation, with pronounced amplitude changes in the time regime up to 100 ps (as marked in Fig. 12a).

3.5.2 Continuum absorption CA1 and CA2

We assign CA1 and CA2 to highly polarizable protons in hydrogen bonding networks (X–H···Y), where a broad IR continuum absorption emerges from the delocalization of the shared proton and fluctuating X–H···Y distances due to a double-minimum potential as well as ultrafast fluctuating electric fields in the proton environment [61–66]. This effect is also known from Zundel cations ($H_5O_2^+$), which show intense IR continuum absorptions [61–64]. The fluctuating electric fields can result from intermolecular hydrogen bond rearrangements between the solvent molecules, which can occur on picosecond timescale down to 500 fs in MeOH-d_4 that is aggregated in partially bifurcated chains of hydrogen bonded molecules [67]. This network is suggested to enable an ultrafast intermolecular charge transport (ps timescale) via several connected solvent molecules via a Grotthuss-like hopping mechanism, i.e. transport of the charge of the free proton via the hydrogen bonding network instead of much slower diffusive motion of the proton itself [68, 69]. The complexity and variability of proton solvation in MeOH is also shown by the coexistence of various proton solvating methanol cluster structures [70].

In addition, also intramolecular hydrogen bonding networks (see below) can induce continuum absorption bands [65, 71–73].

The dynamics and the origin of CA1 and CA2 will be discussed in detail in the following. As it turns out, CA1 and CA2 follow kinetically the chromophore vibrational band kinetics, suggesting the synchronicity of de/protonation- and conformational chromophore dynamics. This includes the long living photoproduct, as indicated by the non-zero amplitude of CA1 at long delay times.

3.5.3 Kinetic analysis

Global analysis of the transient difference spectra is performed via Eq. (1). A triexponential fit yields time constants $\tau_1 = 2.6 \pm 0.6$ ps, $\tau_2 = 21.3 \pm 2.0$ ps and $\tau_3 = 40.0 \pm 5.0$ ps, in good agreement with the results of our transient UV/VIS

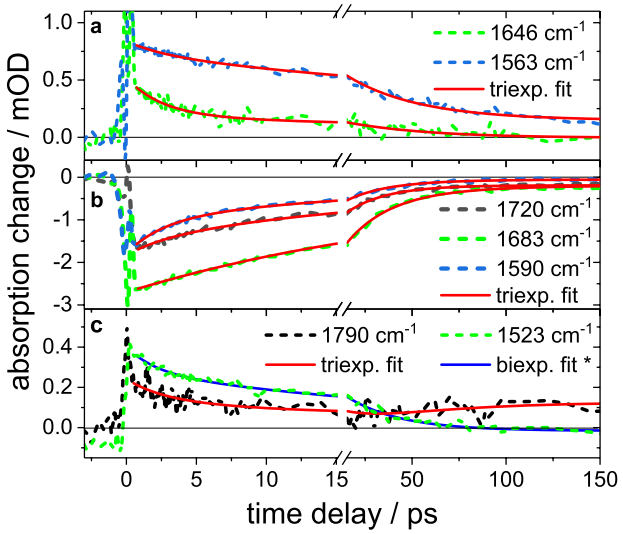

Fig. 13 Mid-IR transient absorption changes at specific probe wavelengths after excitation of PCB at 580 nm together with the result of global triexponential analysis for **a** positive transient absorption changes (product signals), **b** negative transient absorption changes (ground state bleaching bands), and **c** signals in the range of CA1 and CA2* (* biexponential fit, cf. text)

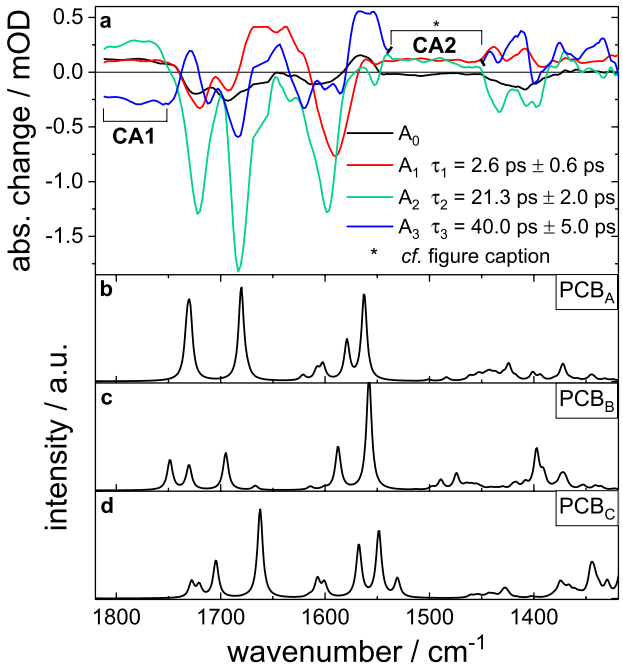

Fig. 14 **a** Decay-associated spectra of the kinetic components of PCB after photoexcitation at 580 nm as result of a triexponential fit. The marked (*) spectral region is fitted biexponentially, resulting in $\tau_{ibiexp} \approx \tau_{itriexp}$ and $A_{ibiexp} \approx A_{itriexp}$ (i = 1, 2). **b–d** Calculated static IR absorption spectra of the ground state species **b** PCB_A, **c** PCB_B and **d** PCB_C, obtained by DFT calculations with polarizable continuum model (same as in Fig. 10)

measurements (cf. 3.2). Figure 13 shows absorbance transients at selected wavenumbers and documents the quality of the fit in the entire spectral range. Note that an analysis of exclusively the spectral range of CA1 (Fig. S4) again yields basically the same three time constants, including a non-zero amplitude for long delay times. In contrast, the spectral region of CA2 (1450–1550 cm^{-1}) exhibits a solely biexponential decay to zero amplitude with $\tau_{1biexp} = 2.4 \pm 0.7$ ps and $\tau_{2biexp} = 29 \pm 6.0$ ps, i.e., similar to τ_1 and τ_2 of the triexponential global (mid-IR-) analysis. It must be noted that these differences strongly suggest different underlying mechanisms for CA1 and CA2 (cf. Sect. 3.5.4).

For the detailed spectro-temporal analysis of the transient difference spectra (Fig. 12) the DAS, resulting from the global analysis, are depicted in Fig. 14a, together with the calculated static IR absorption spectra of the ground state species PCB_A (b), PCB_B (c) and PCB_C (d) (same as in Fig. 10). A more extensive assignment of frequency, intensity and composition of selected IR-vibrational modes on the basis of the DFT calculations (cf. Section 3.4.) is given in Table S1. In the following, a detailed analysis of the photoinduced reactions occurring in the time range of τ_1, τ_2 and τ_3 is given on the basis of the most significant chromophore bands as well as of CA1 and CA2 in $A_{1\text{-}3}$ and in A_0 (cf. Fig. 14). It turns out that the results confirm basic features of the kinetic model presented above, and allow additional diversifications concerning structural dynamics and protonation reactions.

3.5.4 Time range of τ_1

In the time range of τ_1, a negative band at 1590 cm^{-1} is observed in A_1. This band is in good agreement with the strong C=C (5,6) str. vibration band at 1588 cm^{-1} in the calculations for species PCB_B (cf. Fig. 14c). The atom numbers used in the DFT calculations for ground state species PCB_A (similar numbering for PCB_B and PCB_C (cf. Fig. S2 and S3)) are shown in Fig. 16 (notation: (5,6): stretching vibration between atom 5 and 6). Furthermore, the band pattern consisting of the small peak at ca. 1752 cm^{-1} in the early difference spectra in Fig. 12 and the negative bands at 1720 and 1692 cm^{-1} in A_1 is in good agreement with the similar pattern in the calculated spectrum of PCB_B in this region of the carbonyl str. vibrations. This pattern, as well as the negative band at 1590 cm^{-1}, indicate the recovery of PCB_B, supporting the assumption that photo-excited PCB_B (PCB_B*) reacts back to its ground state with the apparent time constant τ_1, in line with our transient UV/VIS measurements.

CA1 and CA2 reveal further complementary insights into the ultrafast photochemistry of PCB. We suggest the instantaneously emerging CA1 and CA2 to result from an ultrafast proton release reaction of PCB_B*, occurring within the system response of 0.38 ± 0.02 ps. In the ground state

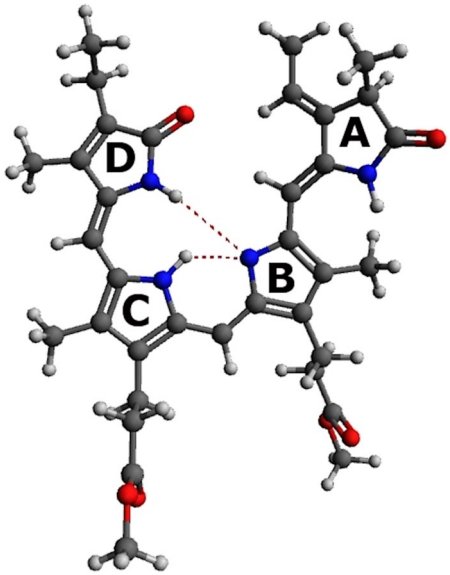

Fig. 15 Molecular structure of the deprotonated form of PCB_B as model for the structure of $PCB_{B,depr}$*. Deprotonation most likely occurs at the nitrogen atom at ring B or ring C. Here, deprotonation at ring B is shown as an example. Dashed: Intramolecular H-bond network, resulting from the deprotonated pyrroleninic nitrogen atom at ring B

species PCB_B, all pyrroleninic nitrogen atoms are assumed to be protonated [15, 18, 28, 32]. Therefore, no intramolecular H-bond network between the pyrroleninic nitrogen atoms is expected. However, after a photoinduced ultrafast proton release reaction, the resulting $PCB_{B,depr}$* is expected to form an intramolecular H-bond network, which, as we suggest here, gives rise to CA2. The molecular structure of $PCB_{B,depr}$*, which is assumed to be similar to the respective PCB_B* form, is depicted in Fig. 15 together with the resulting intramolecular H-bond network. Deprotonation most likely occurs at the nitrogen atom at ring B or ring C, in accordance with Ref. [22, 23].

These assumptions regarding the origin of CA2 are in line with previous studies, i.a. on bacteriorhodopsin and some pyridinium–pyridin systems, which also form intramolecular H-bond networks, inducing IR continuum absorptions. [65, 71–73] The observability of CA2 in the spectral region between ca. 1450–1550 cm^{-1} might be facilitated by the lack of strong vibrational bands in the calculated spectra of PCB_A, PCB_B and PCB_C in this range (cf. Fig. 14).

In contrast to the charged and more stretched PCB_B, which is considered here as the proton donor, the neutral and helical PCB_A is much less prone to deprotonation, in line with its proposed deprotonation on the (slower) picosecond time scale (τ_2) in the model described above (cf. 3.2.).

The proton, released within the system response, is assumed to induce the instantaneously emerging CA1 by interacting with the surrounding solvent molecules, which are aggregated in partially bifurcated hydrogen bonded chains around the solute molecules (cf. above) [67]. Such intermolecular H-bond networks, involving solvent molecules, are well known from Zundel cations [61–64]. Furthermore, a free deuteron, released from the photoacid HPTS in aqueous solution induces a broad continuum absorption above 1750 cm^{-1}, which is fully consistent with our observed CA1 [68].

The assignment of CA1 and CA2 as described above is further backed as follows. The observation of simultaneously emerging CA1 and CA2 strongly suggest that they are initiated by one and the same process. The observation that they exhibit different kinetics points to different underlying physical mechanisms. Thus it does not appear far-fetched, to associate CA1 and CA2 with those two existing molecular environments that are rapidly affected by the deprotonation of PCB_B*: first the solvent shell (released proton, intermolecular H-bond network) and second the moiety of

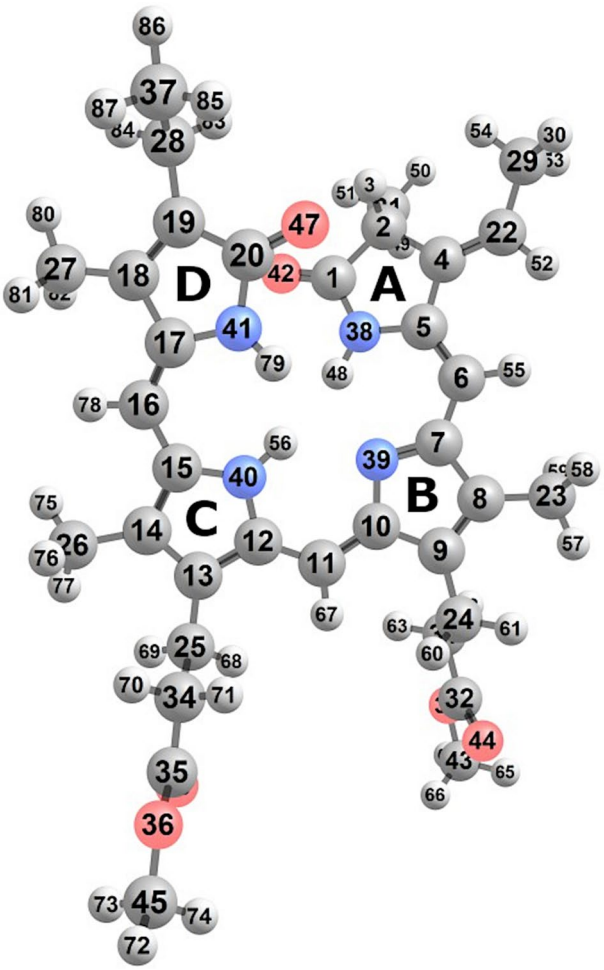

Fig. 16 Molecular structure of PCB_A with the atom numbers used in the DFT calculations for this ground state species (for numbering for PCB_B and PCB_C cf. Fig. S2 and S3)

the pyrroleninic nitrogens ($PCB_{B,depr}$*, intramolecular network, Fig. 15).

In the apparent time range of τ_1, a partial reprotonation of relaxed $PCB_{B,depr}$* ($PCB_{B,depr}$*'), followed by fast decay to PCB_B, is suggested to occur, most likely by geminate recombination with protons remaining within the solvate shell of the respective $PCB_{B,depr}$*' molecule. This is indicated by the partial decay of both CA1 and CA2, i.e. the respective positive amplitudes in A_1 of Fig. 14a. In detail, due to the partial reprotonation reaction, the population of the released protons (causing CA1) decreases, which results in a respective absorption decrease. Furthermore, the reprotonation reaction results in a breakup of the intramolecular H-bond network and thus in a partial decay of CA2. A certain fraction of protons escapes the solvate shell and thus the geminate recombination, leading to a minor, residual population of $PCB_{B,depr}$*' (causing CA2) and of free protons in solution (causing CA1).

3.5.5 Time range of τ_2, long-living photoproduct and A_0

In the time range of τ_2, a partial recovery, resp. formation of ground state PCB_A, PCB_C and PCB_B from PCB_A*, can be deduced as follows.

First, the negative carbonyl band pattern at 1722 and 1683 cm^{-1} in A_2 is in good agreement with the respective carbonyl bands in the calculated IR spectrum of PCB_A (Fig. 14b).

Second, the partial formation of PCB_C is indicated by the shoulder in A_2 at ca. 1662 cm^{-1} and the small negative band at 1553 cm^{-1}. These bands correspond to the bands at 1662 and 1548 cm^{-1} (Fig. 14d), assigned to a C=O (20,47) str. vibration of species PCB_C, and to C=C str. vibrations located at ring B of species PCB_C, respectively.

Third, also for the emergence of species PCB_B, strong indications are found in A_2 by the bands at 1598, 1407 and 1398 cm^{-1}. The appearance of these IR-difference bands with τ_2 reflects the vibronic changes the chromophore undergoes upon the transformation from PCB_A* to PCB_B (as correspondingly in the case for the formation of PCB_A and PCB_C). The band at 1598 cm^{-1} is in very good accordance with the C=C (5,6) str. vibration band at 1588 cm^{-1} in the calculated IR spectrum of PCB_B (Fig. 14c). The small shift in comparison with the respective band in A_1 is most likely owed to its superposition with the strong excited state band around 1650 cm^{-1} in A_1, downshifting the apparent position of the respective negative band. The occurrence of this large difference signal at 1598 cm^{-1} is in good agreement with the assumed rotation around the single bond of the methine bridge between pyrrole ring A and B, changing severely the chemical environment of the C=C (5,6) bond next to it. The negative bands at 1407 and 1398 cm^{-1} are assigned to the absorption bands at 1408 and 1397 cm^{-1} in the calculated IR spectrum of PCB_B (Fig. 14c), carrying contributions of the N–C (39,10) and C–C (9,10) str. vibration, located at ring B (both 1408 cm^{-1}), as well as the N–C (38,5) str. vibration, located at ring A and the C–H rock. vibration of the methine bridges between ring A and B (both 1397 cm^{-1}). These contributions are assumed to be altered strongly by the rotation of ring A, as well as by the breakup of the intramolecular H-bond network, stabilizing PCB_A (cf. [32]) and thus most likely PCB_A*. Thus, the appearance of the bands at 1407 and 1398 cm^{-1} supports the assumed protonation and single bond rotation in the PCB_A* to PCB_B reaction path.

These chromophore vibrational features of A_2 are accompanied by changes of CA1 and CA2. The latter completely decays to zero with $\tau_{2biexp} = \tau_2$ (within error margins) without later changes. Thus, it can be concluded that the intramolecular H-bond network of the (residual) $PCB_{B,depr}$*', causing CA2, must either be screened from the solvent environment [72, 74], or broken up. Here we follow the second possibility and suggest a reaction of $PCB_{B,depr}$*' to a state X* that not only accounts for the decay of CA2 with τ_2 but, in addition, explains and is justified by a number of further observations. This concerns (i) the existence of a long-living species (positive parts in A_0 of UV/Vis and mid-IR data) as a (ii) excited, luminescent state (cf. above, long-living fluorescent component) with (iii) proton acceptor properties and the existence of free protons (non-zero, positive A_0 of CA1) as well as (iv) incomplete PCB_A recovery (negative parts in A_0 of UV/Vis and mid-IR data) on long time scales. A corresponding reaction could be the rotation around the single bond of the methine bridge between the pyrrole rings B and C of $PCB_{B,depr}$*' (cf. Fig. 15), in combination with a deprotonation of the pyrroleninic nitrogen atom at ring B or C. This reaction would induce the breakup of the intramolecular H-bond network (CA2) and resembles the reaction of PCB_A* to PCB_C (cf. Section 3.2. and [28, 32]), suggesting a similar time-scale (i.e. τ_2).

In general, excited state deprotonation is a frequently observed deactivation channel in phytochrome-bound bilin chromophores (e.g. [75]). However, due to a higher conformational flexibility and associated degrees of freedom in the unbound form in solution, competing excited state reactions as proposed above are conceivable to prevent a fast deactivation.

The long life-time of X* can be rationalized by the required rotations around two methine bridge single bonds and a concomitant reprotonation, processes needed for e.g. a direct reaction to PCB_A. In detail: for long timescales, the chromophore absorption bands of A_0 reflect missing PCB_A population, as indicated by the negative band pattern in the carbonyl region (around 1725 cm^{-1} and 1692 cm^{-1}) which is in good agreement with the respective bands in the calculated IR spectrum of PCB_A (for A_0 in UV/Vis data cf. above). The long living counterpart of the missing PCB_A

population is expected to show proton acceptor properties as indicated by the existence of free protons, i.e. the positive CA1 in A_0. Thus, a deprotonation reaction leading to the long-living photoproduct, is necessary.

Two alternative explanations for the formation of a long-living photoproduct should be discussed. First, intersystem crossing (ISC), causing its long lifetime, is not expected due to very low ISC yield ϕ_{ISC} of comparable bilins (PCB-dimethyl-ester: $\phi_{ISC} < 10^{-4}$ [76], BV and BVE: $\phi_{ISC} = 0.004$ and 0.001, resp. [77]). Second, double excitation of excited state population during the short fs pump pulse leading to accumulation of an artificial photoproduct is very unlikely due to sample rotation (cf. Section 2.1.), as well as moderate sample excitation (ca. 5% per excitation pulse). Furthermore, the observation of a long-living species in the time-resolved fluorescence measurements of Bischoff et al. [31] with (intrinsically) very low excitation energy supports this rationale.

Finally, it is noted that CA1 decays in the time range of τ_2 (positive A_2), indicating a net decrease of free protons. Thus, we conclude that the protonation of PCB_A* (yielding PCB_B) is the dominating reaction channel over the deprotonation of PCB_A* (yielding PCB_C) and the deprotonation of $PCB_{B,depr}$*' (yielding the long-living X*).

3.5.6 Time range of τ_3

Here the proposed thermally driven back reaction of the population of PCB_C and PCB_B, formed via decay of PCB_A* to PCB_A into thermal equilibrium [29, 32], involves solely ground state species. This allows to compare both negative (formation of PCB_A) and positive (decay of PCB_B or PCB_C) bands in A_3 directly with the respective calculated ground state absorption spectra (Fig. 14).

Accordingly, in the carbonyl region of A_3, the band pattern with peaks at 1729 (pos.), 1710 (neg.) and 1683 (neg.) cm^{-1}, is consistent with the calculated bands of PCB_C and PCB_A, considering the apparent shift of close lying difference bands.

The positive feature around 1654 cm^{-1} must be assigned to the calculated large absorption band at 1662 cm^{-1} of PCB_C (neither PCB_A nor PCB_B exhibit significant bands in this region), indicating the decay of this species. Moreover, this absorption band of PCB_C originates from the C=O (20,47) str. vibration at ring D, which is severely altered upon the reaction from PCB_C to PCB_A, i.e. the assumed back rotation around the single bond of the methine bridge between ring B and C and the resulting close proximity to the carbonyl group of ring A (cf. Fig. 16). It is thus expected to show as difference band.

The subsequent pattern of three negative bands at 1619 cm^{-1}, 1600 cm^{-1} and 1585 cm^{-1} can be assigned to a respective pattern in the calculated spectrum of PCB_A in the same spectral region, originating from various C=C str. vibrations. The large positive band with two peaks at 1567 and 1553 cm^{-1} is in very good agreement with the absorption bands at 1568 and 1548 cm^{-1} of species PCB_C. They originate from C=C str. vibrations located at ring B and the methine bridge between ring B and C, as well as from the C–C (11,12) str. vibration. The rotation around the latter C–C bond is assumed to be part of the coordinate for the back reaction of PCB_C to PCB_A, causing a change of its frequency. Thus, its appearance as difference band in A_3 is consistent with and additionally corroborates the kinetic model.

Furthermore, the positive band at 1412 cm^{-1} can be assigned to the absorption band at 1397 cm^{-1} in the calculated spectrum of PCB_B, indicating the decay of that species. Finally, further evidence for the decay of PCB_C is given by the broad positive bands at 1375 and 1335 cm^{-1}, which can be assigned to a respective pattern in the calculated spectrum.

Again, the continuum absorption allows deeper insights into the processes occurring in the time range of τ_3. CA1 shows an apparent rise (neg. A_3), indicating a renewed net release of protons via a deprotonation reaction of PCB species. This is in very good agreement with (i) the proposed thermally driven back reaction of PCB_B and PCB_C to PCB_A, involving a deprotonation and reprotonation reaction, respectively, and (ii) the proposed predominant reaction pathway of PCB_A* to PCB_B over PCB_A* to PCB_C in the time range of τ_2.

3.5.7 Extended reaction scheme for PCB in MeOH

In addition to the UV/Vis fs-TA and fluorescence measurements, the mid-IR spectro-temporal behaviour of a multitude of chromophore vibrational bands adds striking evidence for major features of the hitherto proposed reaction scheme on structural grounds. This concerns not only the bands described above, but likewise bands which are observed but not explicitly discussed here. Furthermore, the kinetics of CA1 and CA2 yield new aspects on concomitant de/protonation processes. The totality of the individual observations and their cross-references give us a solid basis for an extended reaction scheme, as described below (Fig. 17).

Excitation with 580 nm leads to PCB_A* and PCB_B*. The latter shows an ultrafast proton release reaction on time scales below the system response (< 0.38 ps), yielding PCB_B*$_{depr}$, followed by a partial reprotonation reaction (most likely geminate recombination) and (very fast) deactivation to PCB_B on the apparent time-scale of τ_1 (cf. Fig. 17a), accompanied by minor fluorescence (cf. Sect 3.3.). A fraction of protons escapes the solvate shell, leaving a residual population of $PCB_{B,\,depr}$*'.

In the time range of τ_2 (cf. Fig. 17b), PCB_A* reacts back to its ground state PCB_A, accompanied by minor

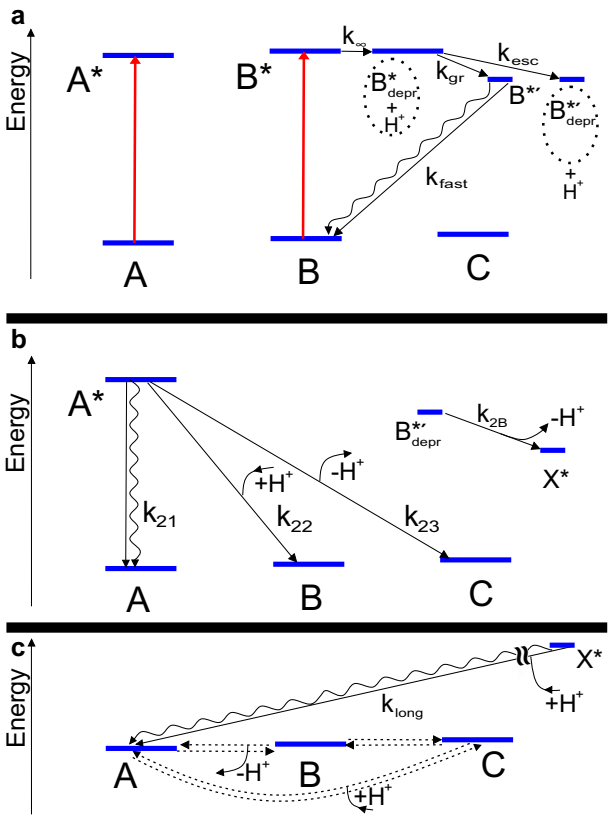

Fig. 17 Extended kinetic scheme of the photoreaction of PCB (as described in the text) after excitation with $\lambda_{exc} = 580$ nm, divided in the time ranges of τ_1 (**a**), τ_2 (**b**) and τ_3, as well as for long time scales (both **c**). Red arrows indicate excitation; straight and wavy lines indicate radiationless and radiative transitions, respectively. Dotted arrows show thermally driven equilibrium reactions of the ground state species. **a** Assuming $k_{fast} >> k_{gr}$, $(k_{gr}+k_{esc})^{-1} = \tau_1$. $k_{inf}^{-1} < 0.38$ ps (system response time). **b** $(k_{21}+k_{22}+k_{23})^{-1} = \tau_2$, $(k_{2B})^{-1}$ is the time constant resulting from the biexponential fit of CA2. **c** The apparent time constant τ_3 is determined by the rate constants governing the thermal equilibration between excess population of B and C with A. For more information cf. main text

fluorescence. Furthermore, PCB_A* reacts in parallel to PCB_B and PCB_C, where the first predominates the latter. These pathways are accompanied by protonation and deprotonation, respectively, as well as a rotation around the single bonds of the methine bridges between ring A and B, and ring B and C, respectively. On the time-scale close to that of τ_2, $PCB_{B,depr}$*' reacts to the long-living photoproduct X*, via an additional deprotonation (leading to a protonation state akin to that of PCB_C) and most likely a rotation around the single bond of the methine bridge between ring B and C.

In the time range of τ_3 (cf. Fig. 17c), a thermally driven back reaction to the thermal equilibrium between the ground state species occurs. In the course of this process, the excess population of PCB_C and PCB_B reacts back to PCB_A, accompanied by a protonation reaction and a deprotonation reaction, respectively.

On long timescales (cf. Fig. 17c), the long-living photoproduct X* possibly reacts back to PCB_A, accompanied by a protonation reaction, two methine bridge single-bond rotations and minor fluorescence, closing the photocycle of PCB.

4 Conclusions

Here we present an in-depth investigation of the primary photoinduced processes of phycocyanobilin in MeOH at room temperature.

First, UV/Vis fs-TA and static fluorescence experiments led to an extension of the existing model [29, 31, 32] for PCB excited state deactivation by proposing the formation of a long-living exited state species, X*, with a nanosecond fluorescence lifetime.

Second, we performed mid-IR fs-TA-measurements, backed by DFT calculations on relative ground state electronic energies and normal mode vibrational analysis of the three suggested PCB species PCB_A, PCB_B and PCB_C. The temporal evolution of chromophore vibrational bands yields a wealth of information on the chromophore conformational dynamics, substantiating the model also on structural grounds.

In addition, the newly observed IR absorption continua CA1 and CA2 are assigned to inter- and intramolecular H-bonded networks, respectively, based on literature data as well as (1) their simultaneous instant rise (consistent with a common initiating process) and (2) their different kinetics (suggesting different underlying physical mechanisms, i.e. molecular environments). Their kinetics reflect various chromophore de/protonation processes, associated with specific chromophore reaction steps. Thereby, strong experimental evidence could be obtained for the proposed disproportionation reaction of excited PCB_A, leading to ground state PCB_B and PCB_C population. Furthermore, PCB_B* is suggested to undergo ultrafast (within instrumental system response) deprotonation, followed by a branched reaction to its ground state upon reprotonation on the one hand and, upon a second deprotonation, to a PCB_C-like excited state and fluorescent species, identified with the long-living product X. On these grounds an extended reaction scheme is proposed.

We here, to the best of our knowledge, describe for the first time the observation of transient spectral IR-continua in MeOH solution after photoexcitation of a dissolved bilin. In this work, we focussed on their potential for the assignment and identification of chromophore de/protonation processes. Moreover, they are an interesting topic in itself, which will be further investigated by future experiments.

Finally, it is noted that the various PCB conformers are shown to exhibit divers and rich photochemistry, including de- and reprotonation processes. This underlines their role as versatile chromophores in photoactive proteins, where steric preselection and optimization of specific reaction paths is facilitated by their complex interaction with the chromophore binding pocket, e.g. with proton donating or accepting amino acid side chains.

Supplementary Information The online version contains supplementary material available at https://doi.org/10.1007/s43630-021-00045-7.

Acknowledgements We thank Wolfgang Gärtner, Jörg Matysik (Univ. Leipzig) and Silvia Braslavsky (Max-Planck-Institute CEC) for helpful discussions and Philip Wolf (TUK), Norbert Michael (TU Berlin) and Nadja Wunsch (KIT Karlsruhe) for technical assistance. Financial support by Research Initiative Rheinland-Pfalz *BioComp* for RD and MT, and by German Research Foundation (DFG—SFB1078 project C2) for MAM are greatly acknowledged.

Funding Open Access funding enabled and organized by Projekt DEAL. Partial financial support was received from Research Initiative Rheinland-Pfalz *BioComp* and the German Research Foundation (DFG—SFB1078 project C2).

Availability of data and material The authors declare that all data and materials as well as software applications, support their published claims and are in accordance with field standards.

Declarations

Conflict of interest There are no conflicts of interest to declare.

References

1. Falk H. (1989). *The chemistry of linear oligopyrroles and bile pigments.* Springer, Berlin
2. Legris, M., Ince, Y. C., & Fankhauser, C. (2019). Molecular mechanisms underlying phytochrome-controlled morphogenesis in plants. *Nature Communications, 10*(1), 5219. https://doi.org/10.1038/s41467-019-13045-0
3. Nagatani, A. (2010). Phytochrome: structural basis for its functions. *Current Opinion in Plant Biology, 13*(5), 565–570. https://doi.org/10.1016/j.pbi.2010.07.002
4. Rockwell, N. C., & Lagarias, J. C. (2010). A brief history of phytochromes. *ChemPhysChem, 11*(6), 1172–1180. https://doi.org/10.1002/cphc.200900894
5. Rockwell, N. C., Su, Y. S., & Lagarias, J. C. (2006). Phytochrome structure and signaling mechanisms. *Annual Review of Plant Biology, 57*, 837–858. https://doi.org/10.1146/annurev.arplant.56.032604.144208
6. Vierstra, R. D., & Zhang, J. (2011). Phytochrome signaling: Solving the Gordian knot with microbial relatives. *Trends in Plant Science, 16*(8), 417–426. https://doi.org/10.1016/j.tplants.2011.05.011
7. Velazquez Escobar, F., Kneip, C., Michael, N., Hildebrandt, T., Tavraz, N., Gärtner, W., et al. (2020). The Lumi-R intermediates of prototypical phytochromes. *The Journal of Physical Chemistry B, 124*(20), 4044–4055. https://doi.org/10.1021/acs.jpcb.0c01059
8. Stepanenko, O. V., Stepanenko, O. V., Shpironok, O. G., Fonin, A. V., Kuznetsova, I. M., & Turoverov, K. K. (2019). Near-Infrared Markers based on Bacterial Phytochromes with Phycocyanobilin as a Chromophore. *International Journal of Molecular Sciences*. https://doi.org/10.3390/ijms20236067
9. Chernov, K. G., Redchuk, T. A., Omelina, E. S., & Verkhusha, V. V. (2017). Near-infrared fluorescent proteins, biosensors, and optogenetic tools engineered from phytochromes. *Chemical Reviews, 117*(9), 6423–6446. https://doi.org/10.1021/acs.chemrev.6b00700
10. Watermann, T., Elgabarty, H., & Sebastiani, D. (2014). Phycocyanobilin in solution—A solvent triggered molecular switch. *Physical Chemistry Chemical Physics, 16*(13), 6146–6152
11. Mizutani, T., & Yagi, S. (2012). Linear tetrapyrroles as functional pigments in chemistry and biology. *Journal of Porphyrins and Phthalocyanines, 08*(03), 226–237. https://doi.org/10.1142/s1088424604000210
12. Schram, B. L., & Kroes, H. H. (1971). Structure of phycocyanobilin. *European Journal of Biochemistry, 19*(4), 581–594
13. Fu, E., Friedman, L., & Siegelman, H. W. (1979). Mass-spectral identification and purification of phycoerythrobilin and phycocyanobilin. *The Biochemical Journal, 179*, 1–6
14. Knipp, B., Müller, M., Metzler-Nolte, N., Balaban, T. S., Braslavsky, S. E., & Schaffner, K. (1998). NMR verification of helical conformations of phycocyanobilin in organic solvents. *Helvetica chimica acta, 81*(5–8), 881–888
15. Rohmer, T., Lang, C., Gärtner, W., Hughes, J., & Matysik, J. (2010). Role of the protein cavity in phytochrome chromoprotein assembly and double-bond isomerization: A comparison with model compounds. *Photochemistry and Photobiology, 86*(4), 856–861. https://doi.org/10.1111/j.1751-1097.2010.00740.x
16. Marai, C. N. J., Chass, G. A., Doust, A. B., & Scholes, G. D. (2004). An ab initio conformational study on 2,3-dihydrobilin-1,19(21H,24H)-dione, a model compound for open-chain tetrapyrroles. *Journal of Molecular Structure: THEOCHEM, 680*(1–3), 219–225. https://doi.org/10.1016/j.theochem.2004.04.040
17. Tu, P., Yao, Y., Li, Y., & Liu, B. (2009). Conformational flexibility of phycocyanobilin: Monte-Carlo and DFT study. *Journal of Molecular Structure: THEOCHEM, 894*(1), 9–13
18. Göller, A. H., Strehlow, D., & Hermann, G. (2001). Conformational flexibility of phycocyanobilin: An AM1 semiempirical study. *ChemPhysChem, 2*(11), 665–671
19. Röben, M., & Schmieder, P. (2011). Assignment of phycocyanobilin in HMPT using triple resonance experiments. *Magnetic Resonance in Chemistry, 130*, 11170–11178
20. van Thor, J. J., Borucki, B., Crielaard, W., Otto, H., Lamparter, T., Hughes, J., et al. (2001). Light-induced proton release and proton uptake reactions in the cyanobacterial phytochrome Cph1. *Biochemistry, 40*(38), 11460–11471
21. Kraskov, A., Nguyen, A. D., Goerling, J., Buhrke, D., Velazquez Escobar, F., Fernandez Lopez, M., et al. (2020). Intramolecular

proton transfer controls protein structural changes in phytochrome. *Biochemistry, 59*(9), 1023–1037. https://doi.org/10.1021/acs.biochem.0c00053
22. Borucki, B., von Stetten, D., Seibeck, S., Lamparter, T., Michael, N., Mroginski, M. A., et al. (2005). Light-induced proton release of phytochrome is coupled to the transient deprotonation of the tetrapyrrole chromophore. *Journal of Biological Chemistry, 280*(40), 34358–34364
23. Osoegawa, S., Miyoshi, R., Watanabe, K., Hirose, Y., Fujisawa, T., Ikeuchi, M., et al. (2019). Identification of the deprotonated pyrrole nitrogen of the bilin-based photoreceptor by raman spectroscopy with an advanced computational analysis. *The Journal of Physical Chemistry B, 123*(15), 3242–3247. https://doi.org/10.1021/acs.jpcb.9b00965
24. Toh, K. C., Stojkovic, E. A., van Stokkum, I. H., Moffat, K., & Kennis, J. T. (2011). Fluorescence quantum yield and photochemistry of bacteriophytochrome constructs. *Physical Chemistry Chemical Physics: PCCP, 13*(25), 11985–11997. https://doi.org/10.1039/c1cp00050k
25. Singer, P., Fey, S., Göller, A. H., Hermann, G., & Diller, R. (2014). Femtosecond Dynamics in the lactim tautomer of phycocyanobilin: A long-wavelength absorbing model compound for the phytochrome Chromophore. *ChemPhysChem, 15*(17), 3824–3831
26. Zienicke, B., Molina, I., Glenz, R., Singer, P., Ehmer, D., Escobar, F. V., et al. (2013). Unusual spectral properties of bacteriophytochrome Agp2 result from a deprotonation of the chromophore in the red-absorbing form Pr. *Journal of Biological Chemistry, 288*(44), 31738–31751
27. Velazquez Escobar, F., Piwowarski, P., Salewski, J., Michael, N., Fernandez Lopez, M., Rupp, A., et al. (2015). A protonation-coupled feedback mechanism controls the signalling process in bathy phytochromes. *Nature Chemistry, 7*(5), 423–430. https://doi.org/10.1038/nchem.2225
28. Göller, A. H., Strehlow, D., & Hermann, G. (2005). The excited-state chemistry of phycocyanobilin: A semiempirical study. *ChemPhysChem, 6*(7), 1259–1268
29. Dietzek, B., Maksimenka, R., Hermann, G., Kiefer, W., Popp, J., & Schmitt, M. (2004). The excited-state dynamics of phycocyanobilin in dependence on the excitation wavelength. *ChemPhysChem, 5*(8), 1171–1177
30. Schmitt, M., Dietzek, B., Hermann, G., & Popp, J. (2007). Femtosecond time-resolved spectroscopy on biological photoreceptor chromophores. *Laser & Photonics Reviews, 1*(1), 57–78
31. Bischoff, M., Hermann, G., Rentsch, S., Strehlow, D., Winter, S., & Chosrowjan, H. (2000). Excited-state processes in phycocyanobilin studied by femtosecond spectroscopy. *The Journal of Physical Chemistry B, 104*(8), 1810–1816
32. Dietzek, B., Fey, S., Matute, R. A., González, L., Schmitt, M., Popp, J., et al. (2011). Wavelength-dependent photoproduct formation of phycocyanobilin in solution: Indications for competing reaction pathways. *Chemical Physics Letters, 515*(1–3), 163–169
33. Chevalier, K., Wolf, M. M. N., Funk, A., Andres, M., Gerhards, M., & Diller, R. (2012). Transient IR spectroscopy and ab initio calculations on ESIPT in 3-hydroxyflavone solvated in acetonitrile. *Physical Chemistry Chemical Physics, 14*(43), 15007–15020
34. Gross, R., Wolf, M. M., Schumann, C., Friedman, N., Sheves, M., Li, L., et al. (2009). Primary photoinduced protein response in bacteriorhodopsin and sensory rhodopsin II. *Journal of the American Chemical Society, 131*(41), 14868–14878
35. Herbst, J., Heyne, K., & Diller, R. (2002). Femtosecond infrared spectroscopy of bacteriorhodopsin chromophore isomerization. *Science, 297*(5582), 822–825
36. Buhl, E., Eberhardt, P., Bamann, C., Bamberg, E., Braun, M., & Wachtveitl, J. (2018). Ultrafast protein response in channelrhodopsin-2 studied by time-resolved infrared spectroscopy. *Journal of Physical Chemistry Letters, 9*(24), 7180–7184. https://doi.org/10.1021/acs.jpclett.8b03382
37. Lukacs, A., Haigney, A., Brust, R., Addison, K., Towrie, M., Greetham, G. M., et al. (2013). Protein photochromism observed by ultrafast vibrational spectroscopy. *The Journal of Physical Chemistry B, 117*(40), 11954–11959. https://doi.org/10.1021/jp406142g
38. Toh, K. C., Stojkovic, E. A., Rupenyan, A. B., van Stokkum, I. H., Salumbides, M., Groot, M. L., et al. (2011). Primary reactions of bacteriophytochrome observed with ultrafast mid-infrared spectroscopy. *Journal of Physical Chemistry A, 115*(16), 3778–3786. https://doi.org/10.1021/jp106891x
39. Esteban, B., Carrascal, M., Abian, J., & Lamparter, T. (2005). Light-induced conformational changes of cyanobacterial phytochrome Cph1 probed by limited proteolysis and autophosphorylation. *Biochemistry, 44*(2), 450–461
40. Peters, F., Herbst, J., Tittor, J., Oesterhelt, D., & Diller, R. (2006). Primary reaction dynamics of halorhodopsin, observed by subpicosecond IR–vibrational spectroscopy. *Chemical physics, 323*(1), 109–116
41. Frisch, M., Trucks, G., Schlegel, H., Scuseria, G., Robb, M., Cheeseman, J., et al. (2016). *Gaussian 09, Revision A.02*. Wallingford: Gaussian Inc.
42. Becke, A. D. (1993). Density-functional thermochemistry. III. The role of exact exchange. *The Journal of chemical physics, 98*(7), 5684. https://doi.org/10.1063/1.464913
43. Tomasi, J., Mennucci, B., & Cammi, R. (2005). Quantum mechanical continuum solvation models. *Chemical reviews, 105*(8), 2999–3094
44. Smallwood, I. (2012). *Handbook of organic solvent properties*: Butterworth-Heinemann.
45. Novak, P., Vikić-Topić, D., Meić, Z., & Sekušak, S., & Sabljić, A. . (1995). Investigation of hydrogen bond structure in benzoic acid solutions. *Journal of Molecular Structure, 356*(2), 131–141
46. Falk, H., Müller, N., & Wansch, S. (1985). Zur Chemie der Pyrrolpigmente, 63. *Mitt. Monatshefte für Chemie/Chemical Monthly, 116*(8–9), 1087–1097
47. Mroginski, M.-A., Németh, K., Bauschlicher, T., Klotzbücher, W., Goddard, R., Heinemann, O., et al. (2005). Calculation of vibrational spectra of linear tetrapyrroles. 3. Hydrogen-bonded hexamethylpyrromethene dimers. *The Journal of Physical Chemistry A, 109*(10), 2139–2150
48. Pulay, P., Fogarasi, G., Pongor, G., Boggs, J. E., & Vargha, A. (1983). Combination of theoretical ab initio and experimental information to obtain reliable harmonic force constants. Scaled quantum mechanical (QM) force fields for glyoxal, acrolein, butadiene, formaldehyde, and ethylene. *Journal of the American Chemical Society, 105*(24), 7037–7047
49. Magdó, I., Németh, K., Mark, F., Hildebrandt, P., & Schaffner, K. (1999). Calculation of vibrational spectra of linear tetrapyrroles. 1. Global sets of scaling factors for force fields derived by ab initio and density functional theory methods. *The Journal of Physical Chemistry A, 103*(2), 289–303
50. Siebert, F., & Hildebrandt, P. (2008). *Vibrational spectroscopy in life science*. John Wiley & Sons.
51. Braslavsky, S. E., Holzwarth, A. R., & Schaffner, K. (1983). Solution conformations, photophysics, and photochemistry of bile pigments; bilirubin and biliverdin, dimethyl esters and related linear tetrapyrroles. *Angewandte Chemie International Edition in English, 22*(9), 656–674
52. Colombano, C. G., Braslavsky, S. E., Holzwarth, A. R., & Schaffner, K. (1990). Fluorescence quantum yields of 124-kDa phytochrome from oat upon excitation within different absorption bands. *Photochemistry and Photobiology, 52*(1), 19–22

53. Schaffner, K., Braslavsky, S. E., & Holzwarth, A. R. (1990). Photophysics and photochemistry of phytochrome. *Advances in Photochemistry, 15*, 229–277
54. Holzwarth, A. R., Braslavsky, S. E., Culshaw, S., & Schaffner, K. (1982). The blue anomalous emission of large and small phytochrome. *Photochemistry and Photobiology, 36*(5), 581–584
55. Holzwarth, A. R., Lehner, H., Braslavsky, S. E., & Schaffner, K. (1978). Phytochrome Models, II. The Fluorescence of Biliverdin Dimethyl Ester1. *Justus Liebigs Annalen der Chemie, 1978*(12), 2002–2017.
56. Rockwell, N. C., Martin, S. S., Feoktistova, K., & Lagarias, J. C. (2011). Diverse two-cysteine photocycles in phytochromes and cyanobacteriochromes. *Proceedings of the National Academy of Sciences, 108*(29), 11854–11859
57. Lim, S., Rockwell, N. C., Martin, S. S., Dallas, J. L., Lagarias, J. C., & Ames, J. B. (2014). Photoconversion changes bilin chromophore conjugation and protein secondary structure in the violet/orange cyanobacteriochrome NpF2164g3' [corrected]. *Photochemical & Photobiological Sciences, 13*(6), 951–962. https://doi.org/10.1039/c3pp50442e
58. Cornilescu, C. C., Cornilescu, G., Burgie, E. S., Markley, J. L., Ulijasz, A. T., & Vierstra, R. D. (2014). Dynamic structural changes underpin photoconversion of a blue/green cyanobacteriochrome between its dark and photoactivated states. *Journal of Biological Chemistry, 289*(5), 3055–3065. https://doi.org/10.1074/jbc.M113.531053
59. Strehlow, D. (2000). *Die primären Photoprozesse im Phycocyanobilin und Phytochrom - Ergebnisse einer vergleichenden Untersuchung*. doctoral thesis, Friedrich-Schiller-University, Jena.
60. Bischoff, M., Hermann, G., Rentsch, S., & Strehlow, D. (2001). First steps in the phytochrome phototransformation: a comparative femtosecond study on the forward (Pr –> Pfr) and back reaction (Pfr –> Pr). *Biochemistry, 40*(1), 181–186. https://doi.org/10.1021/bi0011734
61. Thämer, M., De Marco, L., Ramasesha, K., Mandal, A., & Tokmakoff, A. (2015). Ultrafast 2D IR spectroscopy of the excess proton in liquid water. *Science, 350*(6256), 78–82. https://doi.org/10.1126/science.aab3908
62. Zundel, G. (1994). Hydrogen-bonded chains with large proton polarizability as charge conductors in proteins Bacteriorhodopsin and the F0 subunit of E. coli. *Journal of Molecular Structure, 322*, 33–42. https://doi.org/10.1016/0022-2860(94)87019-5
63. Dahms, F., Fingerhut, B. P., Nibbering, E. T. J., Pines, E., & Elsaesser, T. (2017). Large-amplitude transfer motion of hydrated excess protons mapped by ultrafast 2D IR spectroscopy. *Science, 357*(6350), 491–495. https://doi.org/10.1126/science.aan5144
64. Kampschulte-Scheuing, I., & Zundel, G. (1970). Tunnel effect, infrared continuum, and solvate structure in aqueous and anhydrous acid solutions. *The Journal of Physical Chemistry, 74*(11), 2363–2368. https://doi.org/10.1021/j100705a021
65. Meot-Ner Mautner, M. (2012). Update 1 of: strong ionic hydrogen bonds. *Chem Rev, 112*(10), PR22-103. https://doi.org/10.1021/cr200430n
66. Zundel, G., & Eckert, M. (1989). IR continua of hydrogen bonds and hydrogen-bonded systems, calculated proton polarizabilities and line spectra. *Journal of Molecular Structure: THEOCHEM, 200*, 73–92
67. Pagliai, M., Cardini, G., Righini, R., & Schettino, V. (2003). Hydrogen bond dynamics in liquid methanol. *The Journal of chemical physics, 119*(13), 6655–6662. https://doi.org/10.1063/1.1605093
68. Siwick, B. J., & Bakker, H. J. (2007). On the role of water in intermolecular proton-transfer reactions. *Journal of the American Chemical Society, 129*(44), 13412–13420. https://doi.org/10.1021/ja069265p
69. Morrone, J. A., & Tuckerman, M. E. (2002). Ab initio molecular dynamics study of proton mobility in liquid methanol. *The Journal of Chemical Physics, 117*(9), 4403–4413. https://doi.org/10.1063/1.1496457
70. Kuo, J. L., Fujii, A., & Mikami, N. (2007). Theoretical analyses of the morphological development of the hydrogen bond network in protonated methanol clusters. *Journal of Physical Chemistry A, 111*(38), 9438–9445. https://doi.org/10.1021/jp074676t
71. Rammelsberg, R., Huhn, G., Lubben, M., & Gerwert, K. (1998). Bacteriorhodopsin's intramolecular proton-release pathway consists of a hydrogen-bonded network. *Biochemistry, 37*(14), 5001–5009. https://doi.org/10.1021/bi971701k
72. Rabold, A., Bauer, R., & Zundel, G. (1995). Structurally symmetrical N+H...N <--> N...H+N Bonds. The proton potential as a function of the pKa of the N-Base. FTIR results and quantum chemical calculations. *The Journal of Physical Chemistry, 99*(7), 1889–1895
73. Garczarek, F., & Gerwert, K. (2006). Functional waters in intraprotein proton transfer monitored by FTIR difference spectroscopy. *Nature, 439*(7072), 109–112. https://doi.org/10.1038/nature04231
74. Brzezinski, B., & Zundel, G. (1981). Influence of stereochemistry, screening, and deuteration of long and short intramolecular easily polarizable hydrogen bonds on their infrared continua. *Canadian Journal of Chemistry, 59*(5), 786–794. https://doi.org/10.1139/v81-114
75. Toh, K. C., Stojkovic, E. A., van Stokkum, I. H., Moffat, K., & Kennis, J. T. (2010). Proton-transfer and hydrogen-bond interactions determine fluorescence quantum yield and photochemical efficiency of bacteriophytochrome. *Proc Natl Acad Sci USA, 107*(20), 9170–9175. https://doi.org/10.1073/pnas.0911535107
76. Braslavsky, S. E., Schneider, D., Heihoff, K., Nonell, S., Aramendia, P. F., & Schaffner, K. (1991). Phytochrome models. 11. Photophysics and photochemistry of phycocyanobilin dimethyl ester. *Journal of the American Chemical Society, 113*(19), 7322–7334
77. Land, E. J. (1979). The triplet excited states of biliverdin and biliverdin dimethyl ester. *Photochemistry and Photobiology, 29*(3), 483–487